Lamb Waves and Adaptive Beamforming for Aberration Correction in Medical Ultrasound Imaging

Mozaffarzadeh, Moein; Minonzio, Claudio; de Jong, Nico; Verweij, Martin; Hemm, Simone; Daeichin, Verya

DOI
10.1109/TUFFC.2020.3007345

Publication date
2020

Document Version
Final published version

Published in
IEEE Transactions on Ultrasonics, Ferroelectrics and Frequency Control

This article has been accepted for publication in a future issue of this journal, but has not been fully edited. Content may change prior to final publication. Citation information: DOI 10.1109/TUFFC.2020.3007345, IEEE Transactions on Ultrasonics, Ferroelectrics, and Frequency Control

Lamb Waves and Adaptive Beamforming for Aberration Correction in Medical Ultrasound Imaging

Moein Mozaffarzadeh[1,*], Claudio Minonzio [1], Nico de Jong [1,2], Martin D. Verweij [1,2], Simone Hemm [3] and Verya Daeichin[1]

***Abstract*—Phase aberration in transcranial ultrasound imaging (TUI) caused by the human skull leads to an inaccurate image reconstruction. In this paper, we present a novel method for estimating speed of sound and an adaptive beamforming technique for phase aberration correction in a flat polyvinylchloride (PVC) slab as a model for the human skull. First, the speed of sound of the PVC slab is found by extracting the overlapping quasi-longitudinal wave velocities of symmetrical Lamb waves in the frequency-wavenumber domain. Then, the thickness of the plate is determined by the echoes from its front and back side. Next, an adaptive beamforming method is developed, utilizing the measured sound speed map of the imaging medium. Finally, to minimize reverberation artifacts caused by strong scatterers (i.e. needles), a dual probe setup is proposed. In this setup, we image the medium from two opposite directions, and the final image can be the minimum intensity projection of the inherently co-registered images of the opposed probes. Our results confirm that the Lamb wave method estimates the longitudinal speed of the slab with an error of 3.5% and is independent of its shear wave speed. Benefiting from the acquired sound speed map, our adaptive beamformer reduces (in real-time) a mislocation error of 3.1 mm, caused by an 8 mm slab, to 0.1 mm. Finally, the dual probe configuration shows 7 dB improvement in removing reverberation artifacts of the needle, at the cost of only 2.4 dB contrast loss. The proposed image formation method can be used e.g. to monitor deep brain stimulation procedures and localization of the electrode(s) deep inside the brain from two temporal bones on the sides of the human skull.**

***Index Terms*—Transcranial ultrasound imaging, Lamb waves, adaptive beamforming, sound speed map, deep brain stimulation**

I. Introduction

Transcranial ultrasound imaging (TUI) is a practical tool in neurology and a good candidate to monitor the brain [1, 2]. This imaging modality is cheap, user-friendly, accurate and commercially available nowadays in most of hospitals and clinics [2, 3]. However, the image quality is limited by the strong aberrating effect of the skull bone [4-6]. The sound speed and density are much larger, compared to soft brain tissues, which leads to high reverberations within the skull, large aberrations and a high absorption of the acoustic energy [7-10].

Ultrasound beamforming techniques usually assume a constant speed of sound [11-15], which leads to suboptimal focusing and image quality and accuracy. Over the past decades, researchers have been investigating to compensate the effects of the phase aberration from different perspectives (i.e. developing new algorithms and imaging setups) [16, 18]. A wavevector-frequency domain model of the ultrasound wave propagation from a hemisphere-shaped transducer has been developed, using CT scans of the head, to non-invasively obtain an accurate focusing through the human skull for ultrasound therapy [19]. Thickness and density information obtained from CT images can also be directly used to correct the phase aberration induced by the skull [9, 20, 21]. In a study by Yin Xiangtao and Kullervo Hynynen [22], low frequency ultrasound is used to reduce the effects of the skull. A low frequency, e.g. 250 KHz, results in less attenuation and aberration, which makes the bone more transparent. The drawback of this method is its poor resolution. Another method is the time-reversal aberration correction introduced in [7, 23-25]. These methods usually require an invasive experimental setup for computation of the time reversed signals. A non-invasive time reversal-based technique using a dual-transducer setup has also been reported [5]. This non-invasive extension shows promising results in improving the focal spot, thus the image quality. However, it requires complex multistep modeling and processing and has not yet been used for real time imaging.

The method described by Renzel et al. [26] and implemented in Krautkramers Auto-V technology uses a combination of four transducers mounted on a multifaceted wedge. Two of these probes are oriented obliquely to the sample to launch and receive a longitudinal creeping wave along its surface. These probes provide a measurement of the sound speed. The other pair of probes sends and receives the waves through the sample, providing data for measuring its thickness. The draw back with this system is that the 4-probe technique is very complex, time consuming and very difficult to be applied for TUI. An ultrasound brain helmet has also

*corresponding author: M.Mozaffarzadeh (email: m.mozaffarzadeh@tudelft.nl; phone: +31617673356)

1 Laboratory of Medical Imaging, Department of Imaging Physics, Delft University of Technology, Delft, The Netherlands.

2 Department Biomedical Engineering, Thoraxcenter, Erasmus Medical Center, Rotterdam, The Netherlands.

3 Institute for Medical Engineering and Medical Informatics, School of Life Sciences, University of Applied Sciences and Arts Northwestern Switzerland, Muttenz, Switzerland

This article has been accepted for publication in a future issue of this journal, but has not been fully edited. Content may change prior to final publication. Citation information: DOI 10.1109/TUFFC.2020.3007345, IEEE Transactions on Ultrasonics, Ferroelectrics, and Frequency Control

been designed for simultaneous 3D ultrasound imaging (USI) [27-29]. This helmet is designed in a way that each matrix array helps the other one in phase aberration correction by being a correction source [30]. The cross-correlation of RF signals is also used to this end. The helmet has been used for 3D transcranial Doppler imaging as well [31].

A dual-array ultrasound imaging system has been designed to calculate the approximate aberration of the skull using two arrays placed on the opposing sides of the skull, one on each of the parietal (or temporal) bones. In this system, at each transmission and reception, the information regarding the wavefront achieved on attenuation and phase is used to compensate the phase aberration [5].

In this paper, we report on a method using dispersion curves of the Lamb waves for determining the sound speed in a flat polyvinylchloride (PVC) slab as a model for the human skull. The method benefits from many modes of vibration generated in the frequency range of 1 to 4 MHZ in the plate. Then, the pulse-echo signals are used to measure the thickness of the plate. Finally, an average sound speed map is constructed, and an adaptive delay-and-sum (DAS) beamformer forms a phase compensated image. The proposed image reconstruction scenario is evaluated with simulations and in-vitro experiments. To minimize the reverberation artifact, a dual-probe setup is developed in which the medium is imaged from two opposite directions.

II. Materials and Methods

A. Sound Speed and Thickness Estimation of a Slab

Lamb waves, which are generated once a solid plate is insonified with a wave, are commonly used in non-destructive-testing [32]. The shape of the Lamb waves depends on the frequency, the insonification angle, the thickness of the insonified media and its acoustic properties. Figure 1 shows the Lamb wave dispersion curves for a free plate. Each mode only exists above a certain frequency (called nascent frequency). If we increase the frequency (having other parameters constant), a higher number of modes will be generated as there is no upper frequency limit for any of the modes. At high frequencies, the first symmetric and asymmetric modes (S0 and A0) approach the Rayleigh wave velocity. In contrast, all higher modes approach the shear wave velocity of the plate. At low frequencies, the S0 dispersion curve approaches the quasi-longitudinal wave velocity. The same applies for all the higher S-modes at a certain frequency, where they form a plateau. Generally, only one or very few Lamb wave modes are generated by tuning the excitation frequency (see Figure 1); this happens in the low-frequency range due to the inherent cut-off frequencies of individual modes. This makes it possible to fit the numerical data obtained by Rayleigh-Lamb equations on the generated modes in order to obtain the longitudinal wave speed of the insonified material [33]. The Rayleigh-Lamb equations are:

$$\frac{tan(\beta h/2)}{tan(\alpha h/2)} = -\frac{4\alpha\beta k^2}{k^2-\beta^2} \pm 1,$$
$$\alpha^2 = \frac{\omega^2}{v_l^2} - k^2, \quad (1)$$
$$\beta^2 = \frac{\omega^2}{v_s^2} - k^2,$$

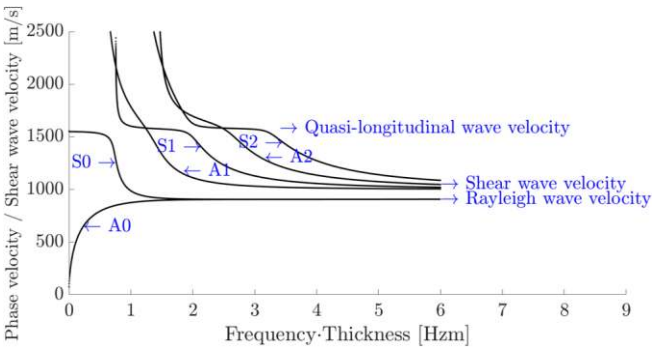

Figure 1. Lamb wave dispersion curves for a free plate with a longitudinal wave speed of 1581 m/s, a shear wave speed of 1000 m/s, and a thickness of 0.2 m [33].

where h is the thickness of the slab, ω is the angular frequency, k is the wave number, v_l is the compression wave speed or longitudinal speed, and v_s is the shear wave speed [34]. The group speed v_g is defined as the slope of the dispersion curve in the frequency-wavenumber domain [34]:

$$v_g = \frac{d\omega}{dk}. \quad (2)$$

With a medical ultrasound frequency range (1-4 MHz), many modes are generated by insonifying a slab having thickness and speed of sound similar to those in human skull. Consequently, fitting becomes very difficult. However, the superposition of the different symmetric modes in the frequency-wavenumber (*f-k*) domain results in a high intensity region where its slope corresponds to the quasi-longitudinal wave speed in the slab. By transferring the temporal-spatial domain data to the *f-k* domain, then fitting a linear line to the high intensity area (distinguishable with a threshold), and finally multiplying the slope of the line by 2π, the speed of sound in the aberration medium can be measured. Thereafter, we can use the reflection from two sides of the slab (Figure 2(b)), obtained with the pulse-echo method shown in Figure 2(a), to measure the thickness of the slab [35].

B. Beamforming

Knowing the thickness of the slab allows us to compensate the phase in the beamforming step. The delay-and-sum (DAS) beamforming technique is described as follows:

$$y_{DAS}(k) = \sum_{i=1}^{M} x_i(k - \Delta_{i,k}), \quad (3)$$

where $y_{DAS}(k)$ is the beamformed data, k is the time index, M is the number of elements of the array, and $x_i(k)$ and $\Delta_{i,k}$ are the received signals and the corresponding time delay for detector i and time index k, respectively [11]. $\Delta_{i,k}$ is calculated based on

This article has been accepted for publication in a future issue of this journal, but has not been fully edited. Content may change prior to final publication. Citation information: DOI 10.1109/TUFFC.2020.3007345, IEEE Transactions on Ultrasonics, Ferroelectrics, and Frequency Control

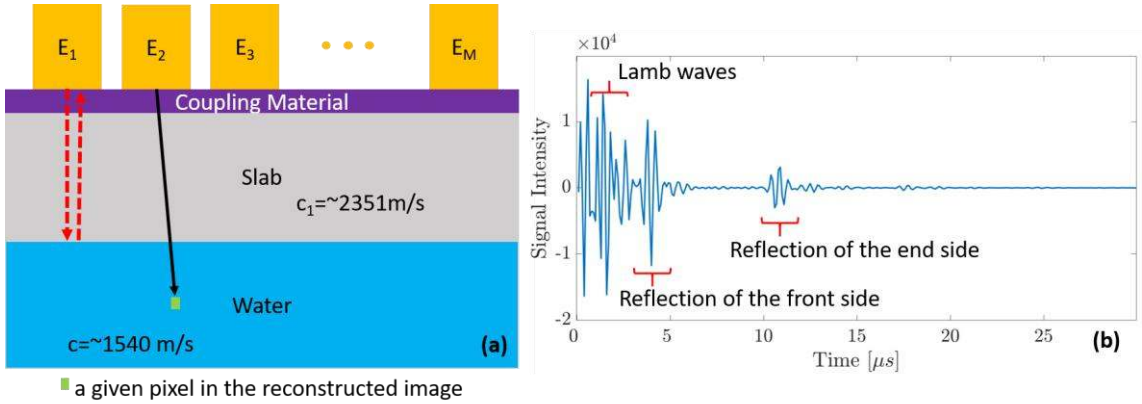

Figure 2. (a) The schematic of the pulse-echo technique (red arrows). The black arrow shows the path connecting an element to a pixel of the reconstructed image. (b) The A-line showing the first and second reflection from two sides of the slab.

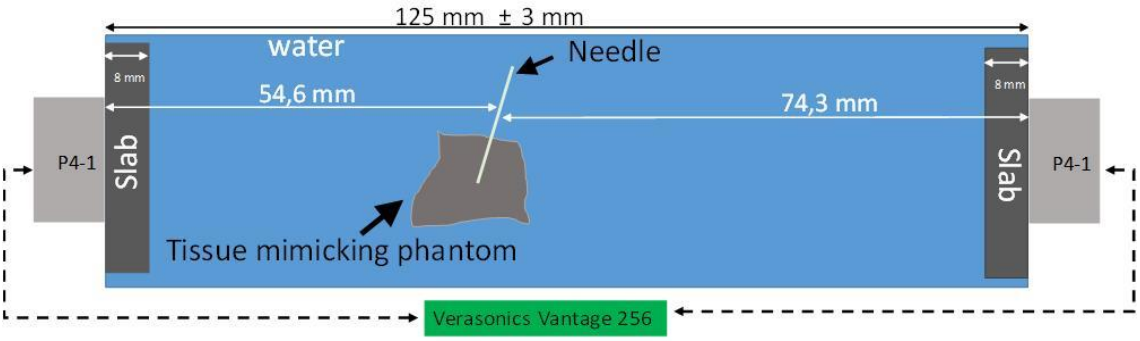

Figure 3. The two-probe experimental setup; the slabs have a sound speed of 2351 m/s and a thickness of 8 mm.

the distance between the location of the i^{th} element of the array and the focused point (indicated by the time index k):

$$\Delta_{i,k} = 2d_{i,k} / c, \tag{4}$$

where $d_{i,k}$ is the one-way distance (between i^{th} element and the focused point) and c is the sound speed (assumed constant) of the imaging medium.

For each pixel (focused point) in the image, we calculate the average sound speed from the transducer elements to the pixel; the black arrow in Figure 2(a) show the path which connect an element to a pixel. An average sound speed map for each element can be obtained using the following equation:

$$v_{avg}(j,k) = (lc_1 c) / \left(cx_{jk} + (l - x_{jk})c_1\right), \tag{5}$$

where j is the index of the element of the array, l is the number of the imaging grid point existing in the vector which connects the j^{th} element to a pixel (black vector in Figure 2(a)), and x_{jk} is the number of imaging grid points having a sound speed of c_1; influenced by the element number (j) and focused point k. To clarify, c is the sound speed of the medium (i.e. brain) and c_1 is the sound speed of the slab. Finally, we can form a corrected B-mode image using the following equations:

$$\Delta_{j,k,corrected} = d_{j,k} / v_{avg}(j,k). \tag{6}$$

$$y_{DAS_{corrected}}(k) = \sum_{j=1}^{M} x_j(k - \Delta_{j,k,corrected}). \tag{7}$$

C. *Numerical Study*

To evaluate the proposed method of longitudinal wave speed estimation, simulations are conducted in the GUIGUW toolbox [36]. The excitation frequency is 1-4 MHz. The shear speed and longitudinal speed are varied from 800 m/s to 1500 m/s and 1500 m/s to 2500 m/s for a slab with a thickness of 8 mm.

D. *Experimental Study*

The experimental setup is shown in Figure 3. It consist of two aligned P4-1 probes (Philips, 2.5 MHz, 96 elements) connected to the Verasonics Vantage 256 system, a needle (1.27 mm diameter) in an agar phantom and two slabs (PVC, 8 mm thick, v_l =2351 m/s) each of which is positioned in front of each probe. The setup with two opposing transducers is designed to image the target from two opposite sides resulting in two images which are intrinsically co-registered. To generate Lamb waves in the slab, element 1 of the array is excited, and all the elements act as a receiver of the Lamb waves. This 2D data set is converted to the frequency-wavelength domain by a 2D FFT.

To evaluate the performance of the Lamb wave method, we have used materials with different longitudinal velocities: polyvinylchloride (PVC; v_l =2351 m/s [37]), polycarbonates (PC; v_l =2220 m/s [38]), polyetheretherketone (PEEK; v_l = 2586 m/s [39]), poly(methyl methacrylate) (PMMA; v_l =2727-2750 m/s [37]) and VeroWhite (VW; v_l =2495m/s). A threshold of -2dB is used to extract the high intensity region in

This article has been accepted for publication in a future issue of this journal, but has not been fully edited. Content may change prior to final publication. Citation information: DOI 10.1109/TUFFC.2020.3007345, IEEE Transactions on Ultrasonics, Ferroelectrics, and Frequency Control

f-k domain.

III. Results

A. Longitudinal Sound Speed Estimation

Figure 4(a) shows the simulation results for frequencies between 1 and 4 MHz and wavenumbers up to 10000 rad/m in a PVC slab of 8 mm thickness. Fitting to a single mode is very difficult, as also proven by the experimental Lamb wave dispersion curves presented in Figure 4(b). However, the symmetric modes overlap and form a high intensity region (red-dashed rectangle in Figure 4(a) and the black-dashed oval in Figure 4(b)) with a specific slope which corresponds to the longitudinal wave speed. The results obtained with different materials are presented in Figure 5(a). Compared to the v_l reported in the literature, the proposed Lamb wave method estimates the v_l with an error up to 3.5%. The dependency of the Lamb wave method to the shear wave speed of the slab is shown in Figure 5(b). The shear wave speed does not affect the v_l estimation; the graphs for v_l =2200 m/s with different shear wave velocities (800 m/s, 900 m/s and 1000 m/s) are overlapped.

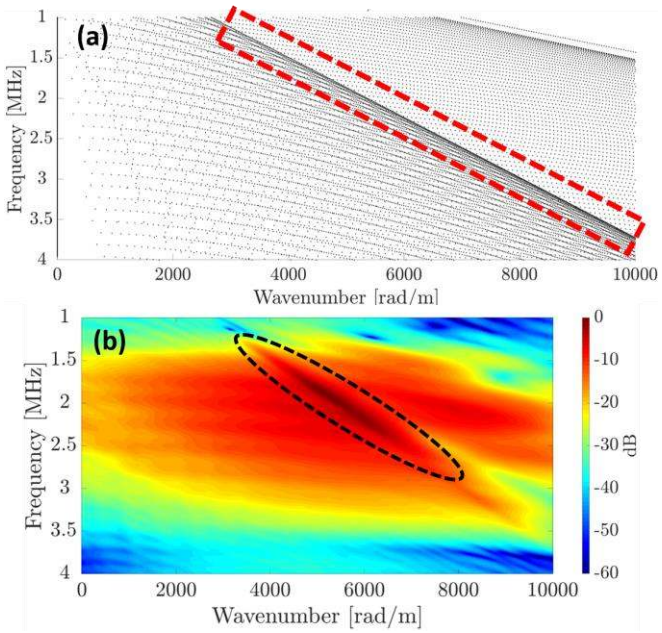

Figure 4. (a) Simulation results obtained by GUIGUW software using a material with the same properties as the PVC slab. (b) Experimental results showing the generation of Lamb waves in a PVC plate (8 mm thickness and a longitudinal speed of about 2351 m/s) using a P4-1 probe with a central frequency of 2.5 MHz. The red-dashed rectangle and black-dashed oval indicate the high intensity area related to the superposition of the different symmetric modes.

B. In-vitro Imaging

Figure 6 shows the images of the needle acquired with the left-side probe, with and without the slab. The phase aberration leads to 3.1 mm error in the location of the needle (red arrow in Figure 6(a)). Using the adaptive beamforming, the target is well-detected at its correct location with an error of 0.1 mm (see Figure 6(c)). The slab causes reverberation artifacts in front of the probe (see Figure 6(b,c)). In addition, we see the reverberation effect of the needle itself (yellow rectangle in Figure 6(a)); due to reflections within the needle [40]. Both the reverberations can be removed using the dual-probe setup shown in Figure 7.

The overlap of these two images can be used to generate a minimum intensity projection (MIP) image which reduces the reverberation artifacts [40, 41]. The MIP image is the minimum intensity of each pixel in the two images acquired by each of the probes. Thanks to our adaptive beamforming technique, the two images seen by the probes are correctly overlapping (compare Figure 7(a) and Figure 7(c)). The tissue mimicking phantom (Figure 7(b), the green arrow) and the needle inside (Figure 7(b), the red arrow) in the MIP image are reconstructed with minimal reverberation artifacts (Figure 7(d)). This results in an MIP image similar to that of obtained in the scenario without any slab (compare Figure 7(b) and Figure 7(d)).

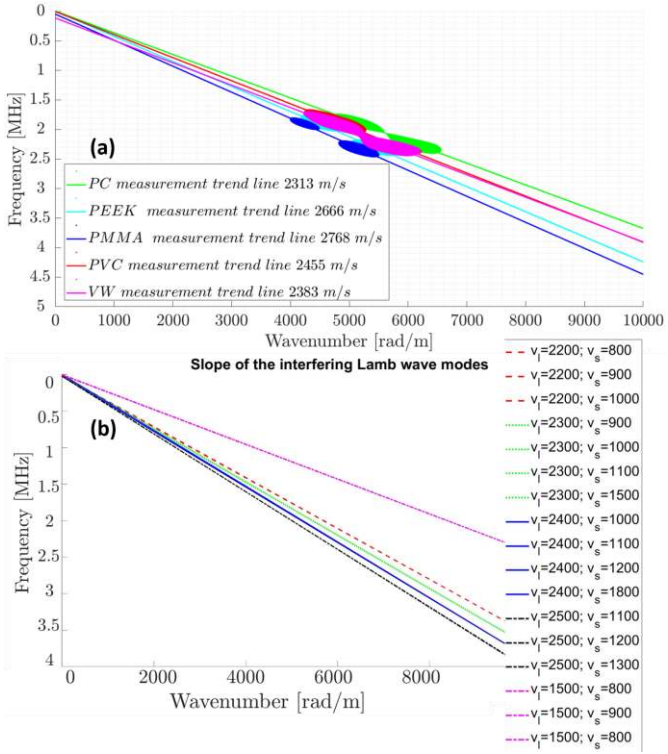

Figure 5. (a) The experimental results obtained with a threshold of -2dB and different materials. (b) The numerical results showing the independency of the Lamb wave method on the shear wave speed of the insonified material.

In order to quantitatively evaluate the performance of the obtained MIP image, we have defined artifact-to-tissue contrast ratio (ATCR) and tissue-to-noise contrast ratio (TTCR) as follows:

$$ATCR = 20 \times \log_{10}(I_{artifact} / I_{tissue}), \quad (8)$$

$$TTCR = 20 \times \log_{10}(I_{tissue} / I_{noise}), \quad (9)$$

where $I_{artifact}$, I_{tissue} and I_{noise} are, as shown in Figure 7(d), the mean amplitude of the needle reverberations artifact (ROI1; blue), mean amplitude of the tissue signal (ROI2; red) and

This article has been accepted for publication in a future issue of this journal, but has not been fully edited. Content may change prior to final publication. Citation information: DOI 10.1109/TUFFC.2020.3007345, IEEE Transactions on Ultrasonics, Ferroelectrics, and Frequency Control

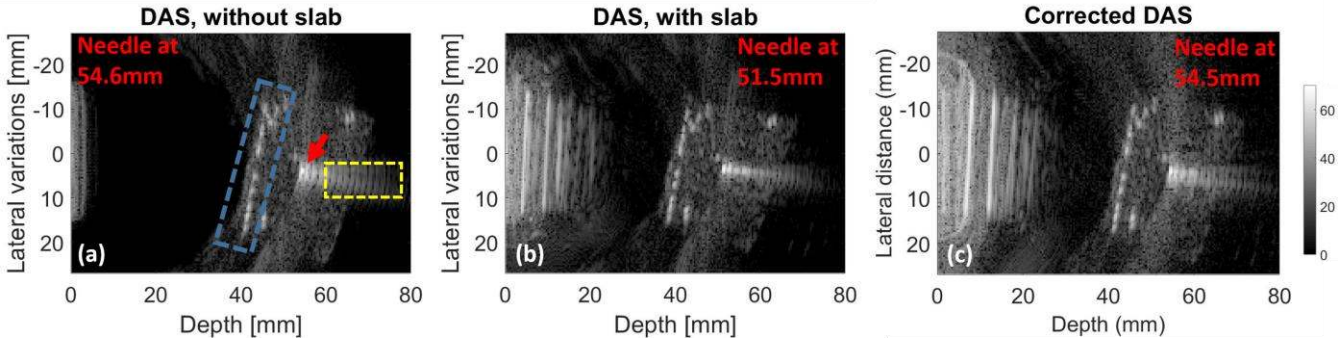

Figure 6. The experimental images using DAS (a) without slab, (b) with slab and (c) with slab and the adaptive beamformer. The red arrow shows the needle. The yellow and blue rectangle show the reverberation effects of the needle and the slab itself, respectively. Images are related to the left probe shown in Figure 3.

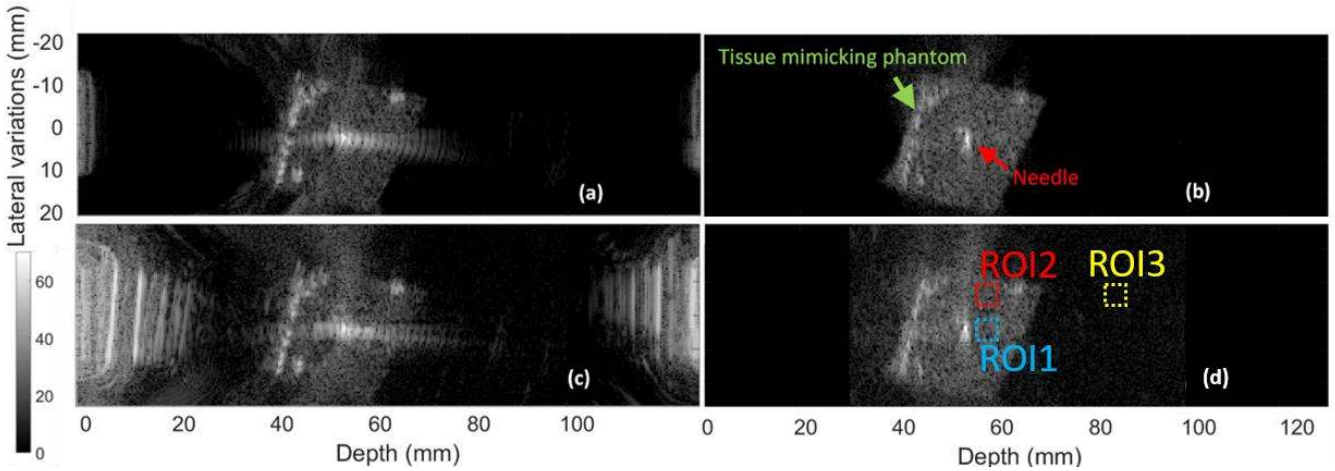

Figure 7. (a) The overlapped image while there is no slab. (b) Minimum intensity projection (MIP) of (a). (c) The corrected overlapped image while there is a slab in front of each transducer. (d) MIP of (c). The ROIs shown in (d) are used to quantitatively evaluate the images.

mean amplitude of the noise (ROI3; yellow). For the corrected overlapped and MIP images (shown in Figure 7(c) and Figure 7(d), respectively), an ARCT of 6.98 dB and -0.03 dB is obtained, respectively, proving that the reverberation artifact is suppressed in the MIP image. A TTCR of 20.04 dB and 17.66 dB is obtained for the corrected overlapped and MIP images, respectively, indicating that the reverberation artifact is suppressed in the MIP image at the expense of a 2.38 dB loss in the image contrast.

IV. Discussion

The availability of a non-invasive real time method for in-vivo measurement of both sound speed and thickness of the human skull bone is of a great benefit to various transcranial ultrasonic imaging and treatment applications. One of such applications is deep brain stimulation (DBS) in which brain function is locally regulated via electrodes implanted deep inside the brain. Accurate implantation of these electrodes in the correct location inside the brain guarantees the successful outcome of the operation [34, 42]. Currently, there is no intraoperative imaging modality guiding the electrode implantation in DBS in real time. In this paper, we created a simple model of DBS electrode monitoring, which we demonstrated by imaging a needle inside an agar phantom at the presence of PVC slabs in front of the probe. The slabs used in front of both transducers are to mimic the human skull since they have similar thickness and sound speed.

Lamb waves are commonly used for non-destructive testing (NDT) [43] to measure material properties such as thickness and speed of sound [44]. When excited with ultrasound pulses used in clinical ultrasound (1-4 MHz), the presence of multiple dispersive modes, especially in materials with speed of sound similar to human skull, complicates the implementations that are used in NDT for material characterization, namely the speed of sound estimation. In this study, we showed that the generation of multiple dispersive modes can be used to extract the longitudinal wave speed of the slab. The overlaps of different symmetric modes in the f-k domain results in a slope which corresponds to the longitudinal wave speed of the material. Linear fitting can be used to find the slope once a threshold is applied on the f-k domain. Our experiments indicated that the estimation error of using a threshold of -2dB is about 3.5%. The numerical results also showed that our technique is independent of the shear wave speed. The same slab but different thicknesses also led to the same slope (the results were not provided). Of note, the PVC slabs used in this study have a constant thickness and a flat surface, which is different from a real skull. The non-

uniform thickness of the skull might prevent the multiple higher-order modes to well overlap- for example due to non-equal-height plateaus- and form a high intensity region. Moreover, the curved structure of the skull might lead to other types of modes, such as the torsional modes, which makes the estimation of the longitudinal sound speed even more complicated. However, we can expect the thickness of the temporal bone (6-9 mm) to be appeared almost flat and with no large inhomogeneities in the sound speed and thickness along the width of the P4-1 probe (2.8 cm).

Knowing the v_l of the slab allowed us to measure the thickness of the slab with the pulse-echo technique. In our work, the final thickness of the slab was obtained by averaging the thicknesses seen by all the elements of the array as the slab was flat. However, in practice where we face inhomogeneous and non-flat samples (i.e. skull), the thickness in front of each individual element can be estimated. This provides an overall shape of the sample. A proper identification and separation of the Lamb waves and the front side reflection is crucial. We used a slab in which the front side reflection and the Lamb waves were separable due to their time of flight. However, in clinical condition, the front side reflections might not be clearly detectable and distinguishable due to the attenuation of skull, its non-uniform shape and the diffusive reflection caused by its surface. Sophisticated signal processing methods can be helpful to address this issue, especially as the Lamb waves and the front side reflection appear in different shapes. Effects of the lens of the probe should be also considered. Moreover, different transmit-receive procedures lead to different round trip trajectories of the front side reflection and Lamb waves. Consequently, aligning the A-lines next to each other shows different trends for Lamb waves and reflections, which can be helpful to separate them.

The estimated speed of sound and thickness of the slab were fed to our adaptive beamformer to correct the phase aberration. To minimize the reverberation artifacts (caused by the slab and the internal reflection of the needle) a dual-probe imaging setup was developed. Once the aberration effect is corrected, a MIP can be applied to the corrected images to obtain an image free of reverberation artifact. Of note, the proposed speed of sound and thickness estimation as well as the adaptive beamforming method do not require a dual probe configuration. Moreover, any sound speed map can be fed to the proposed beamformer, and we are not restricted to the simple model used in this study. The computational complexity of the proposed adaptive beamformer is in the order of the number of elements of the array. To use it in real time, it is necessary to calculate the average sound speed maps (seen by each element of the array) before an operation and then feed the beamformer with these maps during the operation. The speed of sound map and the beam forming algorithm in this study are comprehensive and generic and can be applied to any conditions without any assumption [45]. Calculation of the average sound speed maps might take a few hours due to the large number of combinations between each element of the array and each pixel of the reconstructed image. However, with some simplifications and pre-knowledge of the medium structure, real-time implementation of these calculations will be feasible with a graphical processing unit [46].

The reconstructed images showed that the proposed method effectively compensates the phased aberration caused by the slabs and detects the needle and the boundaries of the agar phantom at their correct locations. Specifically, for the needle, a localization error of 3.1 mm was compensated by the adaptive DAS. Moreover, taking advantages of the dual-probe configuration, the phase-corrected MIP image provided a clear visualization on the needle; about 7 dB improvement in ARCT compared to the simply overlapped images, however, at the expense of 2.38 dB image contrast. The ultrasound probe used in this study was the phased array P4-1 (Philips, 2.5 MHz, 96 elements) as it is widely available, has a proper field of view and its frequency range provides a good compromise between resolution and attenuation. The pitch of such an array should fulfil the Nyquist criterion (smaller than half a wavelength of the Lamb waves), which is the case for P4-1 probe. The smaller the pitch, the better the discrimination of the Lamb waves.

In a follow-up study, we will evaluate the effects of the heterogeneity and non-flat slabs (i.e. hemispherical models) and samples of human skull.

V. Conclusions

We have developed and validated a noninvasive technique, based on Lamb waves, to measure the longitudinal, sound speed, in a slab with a thickness and sound speed similar to those of human skull. Then, an adaptive beamformer was provided to use this information to correct the aberration effect in ultrasound imaging. Our numerical and experimental results showed that the Lamb wave technique detects the correct longitudinal speed (independent of shear speed) within a 3.5% error. Moreover, the proposed beamforming method compensated a mislocation error of 3.1 mm caused by an 8mm thick slab. Our technique, if further validated for human skull, can be used for noninvasive and real-time imaging of the deep brain stimulation electrodes during the operation, thus improving the accuracy of the electrode implantation and therefore improving the outcome of the operation.

Acknowledgment

This work is funded by a joint grant from the Netherlands Organisation for Scientific Research (NWO)/the Netherlands Organisation for Health Research and Development (ZonMw) and the Department of Biotechnology (Government of India) under the program Medical Devices for Affordable Health (MDAH) as Project Imaging Needles (Grant Number 116310008).

REFERENCES

[1] V. L. Babikian *et al.*, "Transcranial Doppler ultrasonography: year 2000 update," *Journal of Neuroimaging,* vol. 10, no. 2, pp. 101-115, 2000.

[2] M. A. O'Reilly, R. M. Jones, and K. Hynynen, "Three-dimensional transcranial ultrasound imaging of microbubble clouds using a sparse hemispherical array," *IEEE Transactions on Biomedical Engineering,* vol. 61, no. 4, pp. 1285-1294, 2014.

[3] R. Kern, F. Perren, S. Kreisel, K. Szabo, M. Hennerici, and S. Meairs, "Multiplanar transcranial ultrasound imaging: standards, landmarks and correlation with magnetic resonance imaging," *Ultrasound in medicine & biology,* vol. 31, no. 3, pp. 311-315, 2005.

[4] M. Tanter, M. Pernot, J.-F. Aubry, G. Montaldo, F. Marquet, and M. Fink, "Compensating for bone interfaces and respiratory motion in high-intensity focused ultrasound," *International Journal of Hyperthermia,* vol. 23, no. 2, pp. 141-151, 2007.

[5] F. Vignon, J. Aubry, M. Tanter, A. Margoum, and M. Fink, "Adaptive focusing for transcranial ultrasound imaging using dual arrays," *The Journal of the Acoustical Society of America,* vol. 120, no. 5, pp. 2737-2745, 2006.

[6] J. Sun and K. Hynynen, "Focusing of therapeutic ultrasound through a human skull: a numerical study," *The Journal of the Acoustical Society of America,* vol. 104, no. 3, pp. 1705-1715, 1998.

[7] K. J. Haworth, J. B. Fowlkes, P. L. Carson, and O. D. Kripfgans, "Towards aberration correction of transcranial ultrasound using acoustic droplet vaporization," *Ultrasound in medicine & biology,* vol. 34, no. 3, pp. 435-445, 2008.

[8] N. M. Ivancevich, G. F. Pinton, H. A. Nicoletto, E. Bennett, D. T. Laskowitz, and S. W. Smith, "Real-time 3-D contrast-enhanced transcranial ultrasound and aberration correction," *Ultrasound in medicine & biology,* vol. 34, no. 9, pp. 1387-1395, 2008.

[9] G. Clement and K. Hynynen, "Correlation of ultrasound phase with physical skull properties," *Ultrasound in medicine & biology,* vol. 28, no. 5, pp. 617-624, 2002.

[10] K. Meyer-Wiethe, F. Sallustio, and R. Kern, "Diagnosis of intracerebral hemorrhage with transcranial ultrasound," *Cerebrovascular Diseases,* vol. 27, no. Suppl. 2, pp. 40-47, 2009.

[11] M. Mozaffarzadeh, A. Mahloojifar, M. Orooji, S. Adabi, and M. Nasiriavanaki, "Double-stage delay multiply and sum beamforming algorithm: Application to linear-array photoacoustic imaging," *IEEE Transactions on Biomedical Engineering,* vol. 65, no. 1, pp. 31-42, 2018.

[12] M. Mozaffarzadeh, M. Sadeghi, A. Mahloojifar, and M. Orooji, "Double-stage delay multiply and sum beamforming algorithm applied to ultrasound medical imaging," *Ultrasound in medicine & biology* vol. 44, no. 3, pp. 677-686, 2018.

[13] I. K. Holfort, F. Gran, and J. A. Jensen, "Broadband minimum variance beamforming for ultrasound imaging," *IEEE transactions on ultrasonics, ferroelectrics, frequency control,* vol. 56, no. 2, pp. 314-325, 2009.

[14] M. Mozaffarzadeh, A. Mahloojifar, V. Periyasamy, M. Pramanik, and M. Orooji, "Eigenspace-based minimum variance combined with delay multiply and sum beamformer: Application to linear-array photoacoustic imaging," *IEEE Journal of Selected Topics in Quantum Electronics,* vol. 25, no. 1, pp. 1-8, 2018.

[15] J.-F. Synnevag, A. Austeng, and S. Holm, "Benefits of minimum-variance beamforming in medical ultrasound imaging," *IEEE transactions on ultrasonics, ferroelectrics, frequency control* vol. 56, no. 9, pp. 1868-1879, 2009.

[16] A. Kyriakou, E. Neufeld, B. Werner, M. M. Paulides, G. Szekely, and N. Kuster, "A review of numerical and experimental compensation techniques for skull-induced phase aberrations in transcranial focused ultrasound," *International Journal of Hyperthermia,* vol. 30, no. 1, pp. 36-46, 2014.

[17] S. Flax and M. O'Donnell, "Phase-aberration correction using signals from point reflectors and diffuse scatterers: Basic principles," *IEEE transactions on ultrasonics, ferroelectrics, frequency control* vol. 35, no. 6, pp. 758-767, 1988.

[18] C. A. Carrascal, S. Aristizabal, J. F. Greenleaf, and M. W. Urban, "Phase aberration and attenuation effects on acoustic radiation force-based shear wave generation," *IEEE transactions on ultrasonics, ferroelectrics, and frequency control,* vol. 63, no. 2, pp. 222-232, 2016.

[19] G. Clement and K. Hynynen, "A non-invasive method for focusing ultrasound through the human skull," *Physics in Medicine & Biology,* vol. 47, no. 8, p. 1219, 2002.

[20] F. Marquet *et al.*, "Non-invasive transcranial ultrasound therapy based on a 3D CT scan: protocol validation and in vitro results," *Physics in Medicine & Biology,* vol. 54, no. 9, p. 2597, 2009.

[21] J.-F. Aubry, M. Tanter, M. Pernot, J.-L. Thomas, and M. Fink, "Experimental demonstration of noninvasive transskull adaptive focusing based on prior computed tomography scans," *The Journal of the Acoustical Society of America,* vol. 113, no. 1, pp. 84-93, 2003.

[22] X. Yin and K. Hynynen, "A numerical study of transcranial focused ultrasound beam propagation at low frequency," *Physics in Medicine & Biology,* vol. 50, no. 8, p. 1821, 2005.

[23] J. Gâteau, L. Marsac, M. Pernot, J.-F. Aubry, M. Tanter, and M. Fink, "Transcranial ultrasonic therapy based on time reversal of acoustically induced cavitation bubble signature," *IEEE Transactions on Biomedical Engineering,* vol. 57, no. 1, pp. 134-144, 2009.

[24] J. Sadler, K. Shapoori, E. Malyarenko, F. Severin, and R. G. Maev, "Locating an acoustic point source scattered by a skull phantom via time reversal matched filtering," *The Journal of the Acoustical Society of America,* vol. 128, no. 4, pp. 1812-1822, 2010.

[25] M. Fink, G. Montaldo, and M. Tanter, "Time-reversal acoustics in biomedical engineering," *Annual review of biomedical engineering,* vol. 5, no. 1, pp. 465-497, 2003.

[26] P. Renzel, "Method for determining the sound velocity in a basic material, particularly for measuring the thickness of a wall," ed: United States patent, 2008.

[27] B. D. Lindsey, E. D. Light, H. A. Nicoletto, E. R. Bennett, D. T. Laskowitz, and S. W. Smith, "The ultrasound brain helmet: new transducers and volume registration for in vivo simultaneous multi-transducer 3-D transcranial imaging," *IEEE transactions on ultrasonics, ferroelectrics, frequency control,* vol. 58, no. 6, pp. 1189-1202, 2011.

[28] S. W. Smith *et al.*, "The ultrasound brain helmet: Feasibility study of multiple simultaneous 3D scans of cerebral vasculature," *Ultrasound in medicine & biology,* vol. 35, no. 2, pp. 329-338, 2009.

[29] B. D. Lindsey, H. A. Nicoletto, E. R. Bennett, D. T. Laskowitz, and S. W. Smith, "Simultaneous bilateral real-time 3-D transcranial ultrasound imaging at 1 MHz through poor acoustic windows," *Ultrasound in medicine & biology,* vol. 39, no. 4, pp. 721-734, 2013.

[30] B. D. Lindsey and S. W. Smith, "Refraction correction in 3D transcranial ultrasound imaging," *Ultrasonic imaging,* vol. 36, no. 1, pp. 35-54, 2014.

[31] B. D. Lindsey *et al.*, "The ultrasound brain helmet for 3D transcranial Doppler imaging," in *2009 IEEE International Ultrasonics Symposium*, 2009, pp. 1395-1398: IEEE.

[32] M. Hong, Z. Su, Y. Lu, H. Sohn, and X. Qing, "Locating fatigue damage using temporal signal features of nonlinear Lamb waves," *Mechanical Systems & Signal Processing,* vol. 60, pp. 182-197, 2015.

[33] N. Ryden, C. B. Park, P. Ulriksen, and R. D. Miller, "Lamb wave analysis for non-destructive testing of concrete plate structures," in *Symposium on the Application of Geophysics to Engineering and Environmental Problems 2003*, 2003, pp. 782-793: Society of Exploration Geophysicists.

[34] H. S. Mayberg *et al.*, "Deep brain stimulation for treatment-resistant depression," *Neuron,* vol. 45, no. 5, pp. 651-660, 2005.

[35] S. H. Tretbar, P. K. Plinkert, and P. A. Federspil, "Accuracy of ultrasound measurements for skull bone thickness using coded signals," *IEEE Transactions on Biomedical Engineering,* vol. 56, no. 3, pp. 733-740, 2009.

[36] P. Bocchini, A. Marzani, and E. Viola, "Graphical user interface for guided acoustic waves," *Journal of Computing in Civil Engineering,* vol. 25, no. 3, pp. 202-210, 2011.

[37] H. A. Afifi, "Ultrasonic pulse echo studies of the physical properties of PMMA, PS, and PVC," *Polymer-Plastics Technology and Engineering,* vol. 42, no. 2, pp. 193-205, 2003.

[38] J. R. Asay and A. H. Guenther, "Experimental determination of ultrasonic wave velocities in plastics as functions of temperature. IV. Shear velocities in common plastics," *Journal of Applied Polymer Science,* vol. 11, no. 7, pp. 1087-1100, 1967.

[39] J. Carlson, J. Van Deventer, A. Scolan, and C. Carlander, "Frequency and temperature dependence of acoustic properties of polymers used in pulse-echo systems," in *IEEE Symposium on Ultrasonics, 2003*, 2003, vol. 1, pp. 885-888: IEEE.

[40] J. Huang, J. K. Triedman, N. V. Vasilyev, Y. Suematsu, R. O. Cleveland, and P. E. Dupont, "Imaging artifacts of medical instruments in ultrasound-guided interventions," *Journal of Ultrasound in Medicine,* vol. 26, no. 10, pp. 1303-1322, 2007.

[41] G. Reusz, P. Sarkany, J. Gal, and A. Csomos, "Needle-related ultrasound artifacts and their importance in anaesthetic practice," *British journal of anaesthesia,* vol. 112, no. 5, pp. 794-802, 2014.

[42] F. Alonso, D. Vogel, J. Johansson, K. Wårdell, and S. Hemm, "Electric Field Comparison between Microelectrode Recording and Deep Brain Stimulation Systems—A Simulation Study," *Brain sciences,* vol. 8, no. 2, p. 28, 2018.

[43] Z. Su and M. Hong, "Nonlinear ultrasonics for health monitoring of aerospace structures using active sparse sensor networks," in *Structural Health Monitoring (SHM) in Aerospace Structures*: Elsevier, 2016, pp. 353-392.

[44] P. Khalili and P. Cawley, "Excitation of single-mode Lamb waves at high-frequency-thickness products," *IEEE transactions on ultrasonics, ferroelectrics, frequency control,* vol. 63, no. 2, pp. 303-312, 2015.

[45] M. Mozaffarzadeh, C. Minonzio, M. D. Verweij, S. Hemm, and V. Daeichin, "Phase Aberration Correction in Transcranial Ultrasound Imaging using Averaged Sound Velocity Map in Delay-and-Sum Beamformer," in 2019 IEEE International Ultrasonics Symposium (IUS), 2019, pp. 1894-1897: IEEE.

[46] S. R. Miri Rostami, M. Mozaffarzadeh, M. Ghaffari-Miab, A. Hariri, and J. Jokerst, "GPU-accelerated double-stage delay-multiply-and-sum algorithm for fast photoacoustic tomography using LED excitation and linear arrays," *Ultrasonic imaging,* vol. 41, no. 5, pp. 301-316, 2019.